JACS Au
AN OPEN ACCESS JOURNAL OF THE AMERICAN CHEMICAL SOCIETY

pubs.acs.org/jacsau
Article

Machine Learning-Driven Insights for Phase-Stable $FA_xCs_{1-x}Pb(I_yBr_{1-y})_3$ Perovskites in Tandem Solar Cells

Ran Luo,◆ Xiangkun Jia,◆ Xiuxiu Niu,◆ Shunchang Liu, Xiao Guo, Jia Li, Zhi-Jian Zhao,* Yi Hou,* and Jinlong Gong*

Cite This: JACS Au 2025, 5, 1771−1780

Read Online

ACCESS | Metrics & More | Article Recommendations | Supporting Information

ABSTRACT: The inherent chemical tunability of perovskite materials has spurred extensive research into composition engineering within the perovskite community. However, identifying the optimal composition across a broad range of variations still remains a significant challenge. Conventional trial-and-error methods are prohibitively expensive and environmentally taxing for comprehensive screening. Here, we employed machine learning-accelerated atomic simulation to guide the design of stable perovskite solar cells absorbers. Our approach entailed training of a neural network (NN) potential using data generated from first-principles calculations, yielding a perovskite NN potential exhibiting high accuracy. Utilizing this NN potential, we constructed a phase diagram for $FA_xCs_{1-x}Pb(I_yBr_{1-y})_3$ (where $0 \leq x \leq 1$ and $0 \leq y \leq 1$, FA denotes formamidinium cation). Integrating this with a band gap diagram, we successfully identified global optimal perovskite compositions for tandem applications with 1.7 and 1.8 eV band gaps. We have identified that all $FA_xCs_{1-x}Pb(I_yBr_{1-y})_3$ with >1.8 eV band gaps are thermodynamically vulnerable to phase segregation and developed a strategy to stabilize thermodynamically unstable phases by suppressing phase segregation kinetics. Finally, theoretical predictions were confirmed by the corresponding experiments. Our results suggest that creating perovskites/Si tandem solar cells with 1.7 eV $FA_xCs_{1-x}Pb(I_yBr_{1-y})_3$ encounters less severe challenges in addressing phase segregation issues than perovskites/perovskites tandem solar cells with 1.8 eV $FA_xCs_{1-x}Pb(I_yBr_{1-y})_3$.

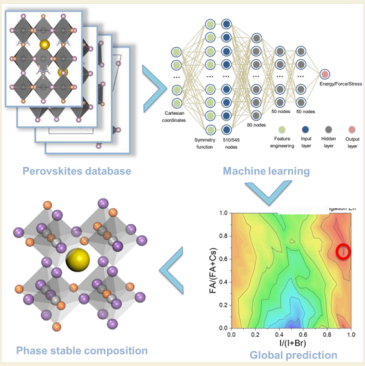

KEYWORDS: *perovskites solar cell, tandem solar cell, machine learning, phase segregation*

1. INTRODUCTION

Organic−inorganic hybrid halide perovskite has emerged as promising material for high-efficiency, low-cost solar cells.[1,2] Distinct from traditional photovoltaic (PV) materials like silicon,[3] perovskite represents a big material family that possesses perovskite-type ABX_3 crystal structure with unfixed compositions. Theoretically, any ions that fit the demand of tolerance factor could be incorporated into the perovskite lattice, which makes perovskite exhibits a remarkable feature, adjustable band gap (from 1.4 to 2.3 eV),[4] which can extend the application of perovskite-based tandem solar cells[5−8] to surpass the Shockley-Queisser (S-Q) efficiency limits.[9,10] The current power conversion efficiency (PCE) of 33.9% achieved by the perovskite/Si tandem cells[11] is already higher than the S-Q limits of all single junction solar cells, thus highlighting the promising future of tandem technology.[12−14] The adjustable band gap of perovskite through compositional engineering mainly originates from the inherent chemical tunability of perovskite materials. Meantime, the corresponding solar cells still can maintain a reasonable power conversion capacity.[15−20] However, band gap adjustment is accompanied by the compositional mixture (especially I−Br mixture), which can cause severe phase segregation inside perovskite to limit the operational stability of tandem solar cells.[5,21−24] Considering that both phase segregation thermodynamics and kinetics are dominated by the chemical composition of perovskite, modulating perovskite composition to find out the appropriate one is critical to perovskite-based tandem solar cells with both high efficiency and stability simultaneously.[25,26]

Given the vast compositional landscape of perovskite-type materials,[27] identifying the optimal composition that could mitigate phase segregation is a crucial yet challenging task in compositional engineering. Traditionally, this process has relied heavily on the experience and intuition of researchers, coupled with experimental trial-and-error methods, which are not only inefficient but also environmentally unfriendly.[28,29] Consequently, the likelihood of finding a globally optimal composition is slim, leading researchers to focus on screening potential compositions within a limited range.[30] The quest for an optimal composition is essentially a complex function of the relationship between the composition and device performance.

Received: January 13, 2025
Revised: February 21, 2025
Accepted: February 24, 2025
Published: March 13, 2025

Machine learning-based computational simulations have emerged as powerful tools for tackling such intricate challenges. An example of this is the successful application of large language models.[31] In the context of perovskite, employing machine learning methods to replace traditional trial-and-error approaches can enable efficient and eco-friendly design of high-performance perovskite absorbers.[32,33] This paradigm shift has potential to markedly shorten the research and development cycle, expediting the commercialization of perovskite-based tandem solar cells. As such, using machine learning to identify compositions that can improve phase stability presents an intriguing and potentially fruitful avenue for the design of perovskite. However, the applications of machine learning in the perovskites usually neglect scientific insights of materials and make predictions simply based on macroscopic properties.[33] Developing a machine learning model that reveals material properties from a basic physical cognition level could be more promising.

Here, we employed the neural network (NN) potential technique[34] to address the functional relationship between atomic structures and system energy. We trained a perovskite NN potential to enable global screening of the commonly used organic−inorganic hybrid halide perovskite system, $FA_xCs_{1-x}Pb(I_yBr_{1-y})_3$, where $0 \leq x \leq 1$ and $0 \leq y \leq 1$. Utilizing the NN-predicted structures, we examined phase segregation through the calculated phase segregation Gibbs free energy. Subsequently, we performed accurate band gap calculations to identify compositions suitable for various tandem solar cells applications. Through this process, we successfully predicted two optimal candidates for perovskite/Si and perovskite/perovskite tandem solar cells. The enhanced PV performance of these candidates, compared with traditional compositions, was corroborated by corresponding experimental validations. This machine learning-driven screening process holds significant promise as a future method for the advanced design of tandem solar cells.

2. METHODS

2.1. Computational Details

The construction of the neural network potential of perovskite materials was performed with LASP code.[35] The training data set was generated by potential energy surface sampling driven by stochastic surface walking (SSW)[36] exploration based on density functional theory (DFT) calculation. Then, during the fitting of the neural network, hyperbolic tangent activation functions were used for the hidden layers, while a linear transformation was applied to the output layer of all networks. The limited-memory Broyden−Fletcher−Goldfarb−Shanno method was used to minimize the loss function to match the DFT energy, force, and stress.

Based on the trained neural network potential, SSW-NN global optimization was utilized to search the optimal atomic structure for each perovskite composition we have considered. We constructed different initial models (perovskite structures with $A_{16}B_{16}X_{48}$ framework) with different ion distributions for each composition and conducted parallel global optimizations. The final chosen structures had the lowest energy among all of the global optimizations. The calculated segregation Gibbs free energy was the mixing Gibbs free energy of pure I and pure Br perovskites with same A sites composition, which contains 16 A sites and 48 X sites totally in our model (details in the SI).

The NN-based variable-cell double-ended surface walking (VC-DESW) method[37] was employed to locate the optimal phase segregation pathways. The initial states of phase segregation were structures predicted by global optimization, while the final states were constructed by separating the Br and I spatially. The calculation was carried out within the SSW-RS framework[38] as implemented in LASP software. The accurate transition structures were located by the constrained Broyden dimer method (CBD).[39]

Spin-polarized DFT calculations were performed using the Vienna Ab initio Simulation Package (VASP)[40] to generate the training data for the neural network. The electron−ion interaction was represented by the projector augmented-wave approach[41,42] using the Perdew−Burke−Ernzerhof (PBE) generalized-gradient approximation (GGA).[43] The plane-wave energy cutoff was set to 320 eV. The first Brillouin zone k-point sampling utilized the γ point only. The energy and force criteria for convergence of the electron density and structure optimization are set at 10^{-6} eV and 0.02 eV $Å^{-1}$, respectively. We constructed 40 initial structures with different compositions (Table S1) and conducted 200 steps of DFT + SSW global optimization to sample the potential energy surface. 602351 structures were collected from the global optimization trajectories. 20500 structures were randomly chosen from the database as the training data set for the neural network. We further conducted high-accuracy electronic self-consistent calculations. The plane-wave energy cutoff was increased to 520 eV. The first Brillouin zone k-point sampling utilized $5 \times 5 \times 5$ γ-centered mesh grid to ensure the accuracy of predicted energy, force, and stress.

2.2. Experimental Details

The patterned ITO glass substrates were wiped with soap water, then ultrasonically washed with deionized water, acetone, and isopropanol for 30 min each. After ultraviolet ozone treatment for 15 min, the substrates were transferred to a nitrogen glovebox. Then, the Me-4PACz (1 mg/mL in IPA) was spin-coated on top of the substrates at 4000 r.p.m. for 30 s and heated at 100 °C for 10 min. The perovskites (predicted 1.7 eV PVK: $Cs_{0.37}FA_{0.63}Pb(I_{0.88}Br_{0.12})_3$, reference 1.7 eV PVK: $Cs_{0.17}FA_{0.83}Pb(I_{0.7}Br_{0.3})_3$, predicted 1.8 eV PVK: $Cs_{0.37}FA_{0.63}Pb(I_{0.69}Br_{0.31})_3$, reference 1.8 eV PVK: $Cs_{0.3}FA_{0.7}Pb(I_{0.6}Br_{0.4})_3$, and predicted 1.59 eV PVK: $FA_{0.90}Cs_{0.10}Pb(I_{0.90}Br_{0.10})_3$) were dissolved in the mixed solvent of DMF:NMP (V:V = 960:150). The 1.0 M perovskite precursor solution was shaken overnight to make it fully dissolved and then used for preparing perovskite films. For the spin-coating process, the substrate was spun at 5000 r.p.m. for 40 s with an acceleration of 5000 rpm/s and N_2 gas was blown on top of the spinning substrates after 20 s. The perovskite films were preannealed at 70 °C for 2 min in N_2-glovebox and then annealed at 150 °C for 10 min in 30% relative humidity. Lastly, C60 (20 nm)/BCP (8 nm)/Ag (100 nm) were deposited to complete the device fabrication.

3. RESULTS AND DISCUSSION

3.1. The Establishment of Neural Network Potentials for Perovskites

Classical first-principles calculations are prohibitively expensive for global screening due to their high computational cost, which contradicts our goal of enhancing screening efficiency. To address this challenge, we have leveraged neural network potential technique to learn the data generated from first-principles calculations, which is an advanced computational technique that uses artificial neural networks to model the potential energy surfaces of atomic systems. It enables highly accurate and efficient simulations of complex materials and chemical reactions by learning from large data set of quantum mechanical calculations. However, our targeted hybrid perovskite system involves seven elements (H, C, N, Cs, Pb, I, and Br), resulting in an exceptionally complex potential energy surface. Therefore, the primary challenge lies in training a neural network capable of accurately capturing this complexity. We have trained a neural network on a data set generated by SSW exploration[36] based on DFT calculations. A neural network (configuration: 545/510-80-50-50-1) with customized feature engineering was constructed to learn the training data set to finally obtain the perovskite NN potential.

https://doi.org/10.1021/jacsau.5c00033
JACS Au 2025, 5, 1771−1780

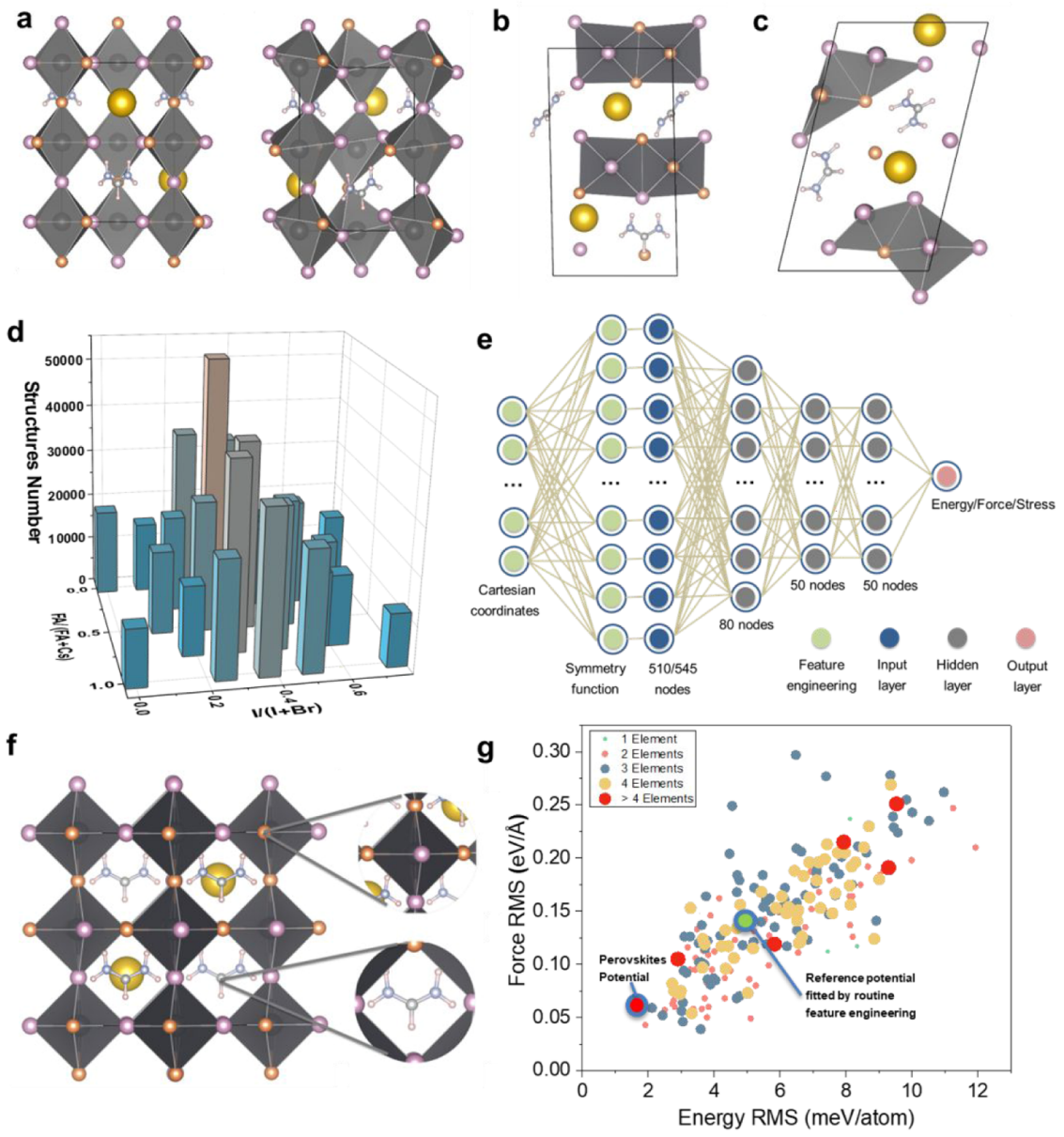

Figure 1. Structures included in the training data set: (a) 3D perovskite structures; (b) 2D perovskite structures; (c) nonperovskite structures. (d) Constitution of training data set. (e) Neural network framework with nodes denoted as spheres and weights denoted as yellow lines. (f) Scheme of two kinds of local chemical environments in perovskite (pink: I; orange: Br; gray: Pb; yellow: Cs; blue: N; light gray: C; white: H). (g) Comparison of the root-mean-square (RMS) error of fitted neural network potential with the potentials that already have been released as well as perovskite potential fitted by routine feature engineering.

We started our efforts with the construction of a training data set (Figure S1). The perovskite structures database was established through density functional theory (DFT) calculations. We constructed initial structures with different compositions and conducted global optimization to sample the potential energy surface and collect structures as training data set. By limiting different parameters (e.g., the lattice constants and atoms positions), we could obtain different types of structures. The predominant type comprises perovskite structures with varying tilt degrees of octahedron (Figure 1a), which can be further categorized into cubic and tetragonal phases. Besides, 2D perovskite (Figure 1b) was also included in the training data set to account for scenarios where the cations are oversized. To ensure the NN can accurately predict the information on the potential energy surface comprising the 7 elements, nonperovskite structures were also incorporated into the training data set, with a randomly selected example depicted in Figure 1c. The final structures database contains 602351 structures, ensuring adequate sampling (detailed information in Table S1). As shown in Figure 1d, all possible compositions of targeted perovskite systems were considered in the database. Thereinto, due to the maximum microstate numbers, we increased the proportion of compositions in which FA/Cs and I/Br approach 1. Through the above efforts, we have constructed the large database containing comprehensive information of the potential energy surface. Finally, 20500 structures were randomly chosen from the database as the training data set for the neural network.

A neural network is further constructed to learn the training data. As shown in Figure 1e, we utilized a very large and deep

https://doi.org/10.1021/jacsau.5c00033
JACS Au 2025, 5, 1771−1780

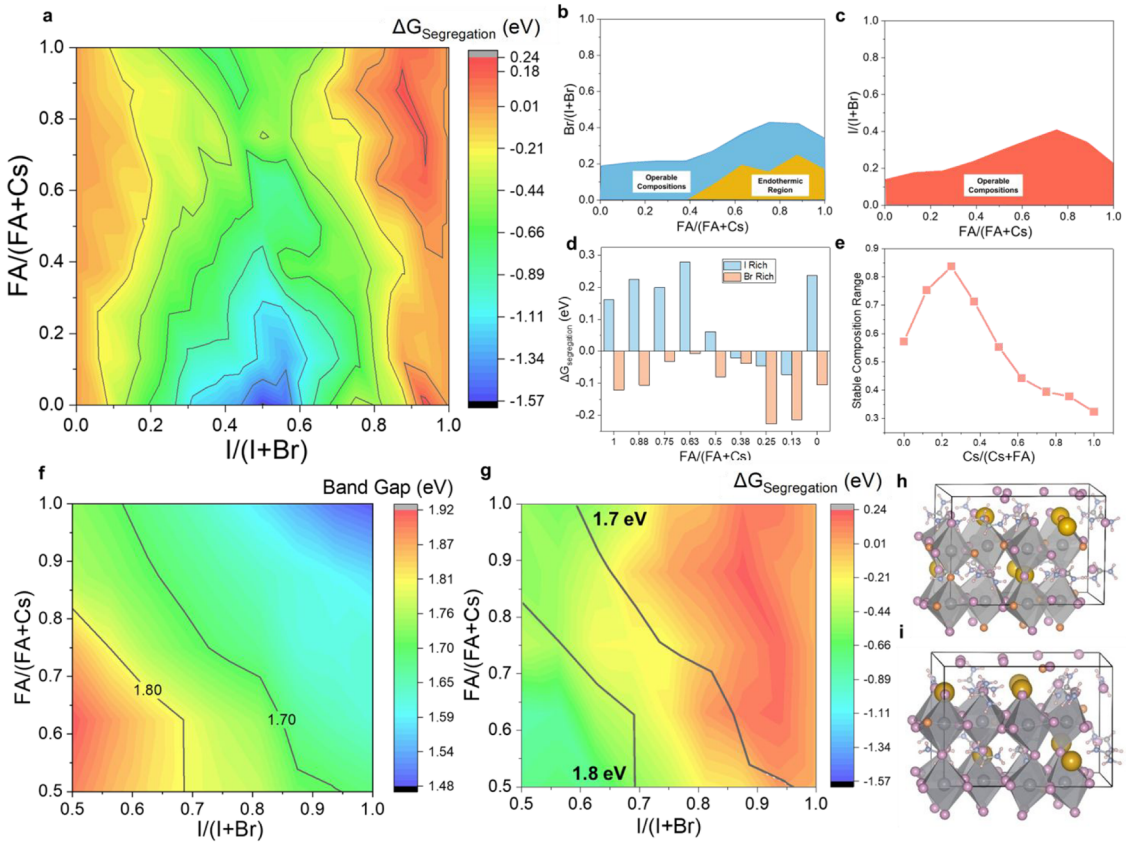

Figure 2. (a) Neural network predicted halides perovskites ($FA_xCs_{1-x}Pb(I_yBr_{1-y})_3$) phase diagram with phase segregation Gibbs free energy as targeting property. (b) Operable and endothermic compositions range for I-rich perovskites. (c) Operable composition range for Br-rich perovskites. (d) Peak values of segregation Gibbs free energies for I-rich and Br-rich perovskites with different A site compositions. (e) Proportion of stable compositions versus addition amount of Cs. (f) Calculated band gap diagram. (g) Perovskites with 1.7 and 1.8 eV band gaps in the predicted phase diagram. (h) Predicted optimal 1.8 eV perovskites. (i) Predicted optimal 1.7 eV perovskites.

network with 3 hidden layers to ensure its capacity to comprehend the complexities of the perovskite system. The critical determinant of the network's accuracy lies in feature engineering, which transforms geometric information from various structures into a mathematical language suitable for learning. We used the power type symmetry functions (PTSDs)[44,45] known for their efficient and accurate feature recognition capabilities. Compared with traditionally used atom-centered symmetry functions,[37] the usage of power radial function in PTSDs could create radial distributions with flexible peak and shape, recognizing atomic features more efficiently. However, the choice of parameters for different functions such as the cutoff radius is largely empirical. We propose to construct PTSDs according to the local chemical environment of the central elements to improve feature recognition. As shown in Figure 1f, perovskites typically exhibit two distinct local chemical environments: the center of cuboctahedral cage occupied by A site cation and the PbX_6 octahedron. Therefore, we established two series of PTSDs tailored to the different geometric characteristics of these environments comprising 510 and 545 symmetry functions, respectively (Tables S2−S3). Leveraging a meticulously designed neural network and a comprehensive training data set at the big data level, we finally trained the complex 7-element neural network potential and realized top accuracy for both energy (1.91 meV/atom) and force prediction (0.064 eV/Å) (Table S4) when compared with other known neural network potentials (Figure 1g). We also fitted a neural network potential using routine feature engineering with the same training data set and fitting epochs, the accuracy of which is far behind our potential with customized feature engineering (Figure 1g). Test on the validation set shows the RMS error could still be maintained at 4.33 meV/atom (energy) and 0.055 eV/Å (force) (Table S5). These results validate the efficacy of our approach and furnish a robust tool for our subsequent theoretical design of perovskites absorber.

3.2. The Thermodynamics of Phase Segregation of Hybrid Perovskites

Clarifying the atomic structures of perovskites is a prerequisite of property prediction. We conducted NN potential-driven global stochastic surface walking (SSW)[36] optimization for 153 perovskites (perovskites structures with $A_{16}B_{16}X_{48}$ framework) with different uniformly distributed FA/Cs and I/Br to obtain the most stable structures for each composition (Figures S2−S3). The final chosen structures had the lowest energy among all of the global optimizations. The utilization of the NN potential has prominently accelerated the calculation speed. For the used model with 192 atoms, performing local optimization through DFT needed 9216 core hours, while NN could finish the calculation in 4.8 s, which shows the superiority of NN in the calculation of large and complex systems. Based on the 153 optimized structures, we tend to investigate the intrinsic phase segregation tendency, which has been seen as a key stability issue that needs to be addressed for future high-efficiency perovskite solar cells. Therefore, we

https://doi.org/10.1021/jacsau.5c00033
JACS Au 2025, 5, 1771−1780

calculated the preference for I and Br to remain in the uniformly mixed state or to be segregated for different compositions using phase segregation Gibbs free energy analysis. As shown in Figures 2a and S4−S5, the collective segregation of Gibbs free energies constitutes the perovskites phase diagram, providing a global perspective on the property of the hybrid perovskites for the first time and help researchers unify the traditional local cognition of certain perovskites compositions.

In the phase diagram, the red region indicates compositions in which the segregation reaction is endothermic, signifying a preference for perovskites to remain in the uniformly mixed state. The yellow region denotes a transition to slightly exothermic segregation reactions, while green and blue regions signify highly exothermic reactions.

Analysis of the phase diagram reveals a notable trend: for each A site composition, as I/Br approaches 1, perovskites exhibit the strongest preference for segregation. This observation is in accordance with the perception that the addition of Br tends to induce phase segregation. Further, the largest red region on the phase diagram corresponds to the I-rich FA-rich phase, a composition extensively studied in the perovskite community.[46−55] This result denotes that our calculation generates a result that is in accordance with the trial-and-error method. We have the same basic cognition about the stability of the perovskite phase as previous researchers.

In addition to confirming existing knowledge, the phase diagram also unveils insights that are challenging to be obtained via the traditional trial-and-error method. Our aim is to provide valuable guidance to researchers prior to synthesizing perovskite solar cells. Normally, maintaining the segregation as an endothermic process could suppress phase segregation. However, if other demands for the perovskites, such as specific band gap values, necessitate choosing compositions with exothermic segregation Gibbs free energies, we recommend controlling them to moderately exothermic levels and relying on kinetics to mitigate the segregation process. According to these perspectives, we defined the compositions with slightly exothermic segregation Gibbs free energy (>−0.4 eV) as operable compositions. We have delimited the boundary of operable compositions for both I-rich perovskites (Figure 2b) and Br-rich perovskites (Figure 2c), recommending researchers synthesize perovskites inside these defined regions. While both I-rich and Br-rich perovskites exhibit operable regions of similar sizes, a notable distinction arises: exothermic compositions are exclusive to I-rich perovskites, whereas all Br-rich perovskites exhibit negative segregation Gibbs free energy. As shown in Figure 2d, I-rich perovskites display significantly higher peak values of segregation Gibbs free energy for each A site composition compared to Br-rich perovskites. Therefore, the I-rich phases exhibit greater stability than Br-rich phases, there remains substantial potential for the utilization of Br-rich phases following the development of efficient kinetic modifications.

For A site composition, when the concentration of Cs in A site is below 40%, the addition of Cs effectively mitigates the segregation preference (as indicated by the green region in the phase diagram). In essence, the addition of Cs enhances the tolerance of the perovskite to the Br, allowing for the incorporation of greater amounts of Br into the perovskite while maintaining the uniformly mixed state. This effect is most pronounced at around 20% Cs concentration (Figure 2e), with only perovskites with 40−60% I demonstrating severe segregation. Moreover, the addition of Cs amplifies the peak value of the segregation energy, with the two highest peaks observed for perovskites containing 90% FA and 90% I, and 60% FA and 90% I, respectively. However, it is noteworthy that the maximum allowable Cs concentration is 40%; exceeding this threshold results in a notable reduction in the segregation Gibbs free energy. This phenomenon may be attributed to a decrease in the tolerance factor when an excessive amount of Cs is presenting in the lattice.

To determine the optimal perovskite composition for different tandem solar cells, band gap is necessary information. Accordingly, we further calculated band gaps (details in Figures S6−S8) in a commonly used compositions range ($0.5 \leq FA/(FA + Cs) \leq 1$, $0.5 \leq I/(I + Br) \leq 1$). As shown in Figure 2f, the band gaps increase from the I-rich to Br-rich phases as well as from the FA-rich phases to the Cs-rich phases. Thereinto, we screened perovskites with 1.7 and 1.8 eV band gaps, which are potential candidates for Si/perovskite tandem and perovskite/perovskite tandem, respectively. Upon marking all of the compositions with 1.7 and 1.8 eV band gaps in the band gap diagram, we observed 1.7 eV perovskite showing a wider composition range for selection, accommodating candidates with both high I concentration and low I concentration. Conversely, the choices of compositions for 1.8 eV perovskites are limited, necessitating the addition of more Br into the perovskites to achieve the desired band gap.

Combining the prediction of both the phase diagram and the band gap diagram (Figure 2g), we have identified optimal perovskite compositions. For 1.7 eV perovskite, the optimal composition of $FA_{0.63}Cs_{0.37}Pb(I_{0.88}Br_{0.12})_3$ is situated in the deep red region of the phase diagram (Figure 2h). However, for 1.8 eV perovskite, the optimal composition ($FA_{0.63}Cs_{0.37}Pb(I_{0.69}Br_{0.31})_3$) (Figure 2i) still locates in the yellow region, indicating that non-1.8 eV perovskite could suppress phase segregation thermodynamically. All of the segregation reactions of 1.8 eV perovskites are exothermic reactions. From this perspective, development of Si/perovskite tandem utilizing 1.7 eV perovskite is more promising. For the perovskite/perovskite tandem that uses 1.8 eV perovskite, a new combination of A sites cations and X sites halogens still needs to be explored to change the thermodynamics of the segregation reaction.

Further convex hull analysis confirms the predicted compositions located on the vertex of the convex hull with $E_{hull} = 0$ eV (Figure S9), which means the compositions have promising internal stability. Meantime, we also noticed that there are some compositions located in the FA-rich I-rich area but have positive E_{hull} values. Though these compositions have positive segregation Gibbs free energy, they will still suffer from internal instability in the practical application, which needs specific attention.

3.3. The Kinetics of Phase Segregation of Hybrid Perovskites

Kinetics can serve as another efficient way to suppress the phase segregation process, especially for the perovskites with a high Br concentration. Given the favorable segregation thermodynamics observed in Br-rich perovskites, reliance on a high activation barrier becomes imperative to retard the segregation reaction. As our predicted 1.8 eV candidate exhibits exothermic segregation Gibbs free energy, possessing a high activation barrier will be very important to the stability

https://doi.org/10.1021/jacsau.5c00033
JACS Au 2025, 5, 1771−1780

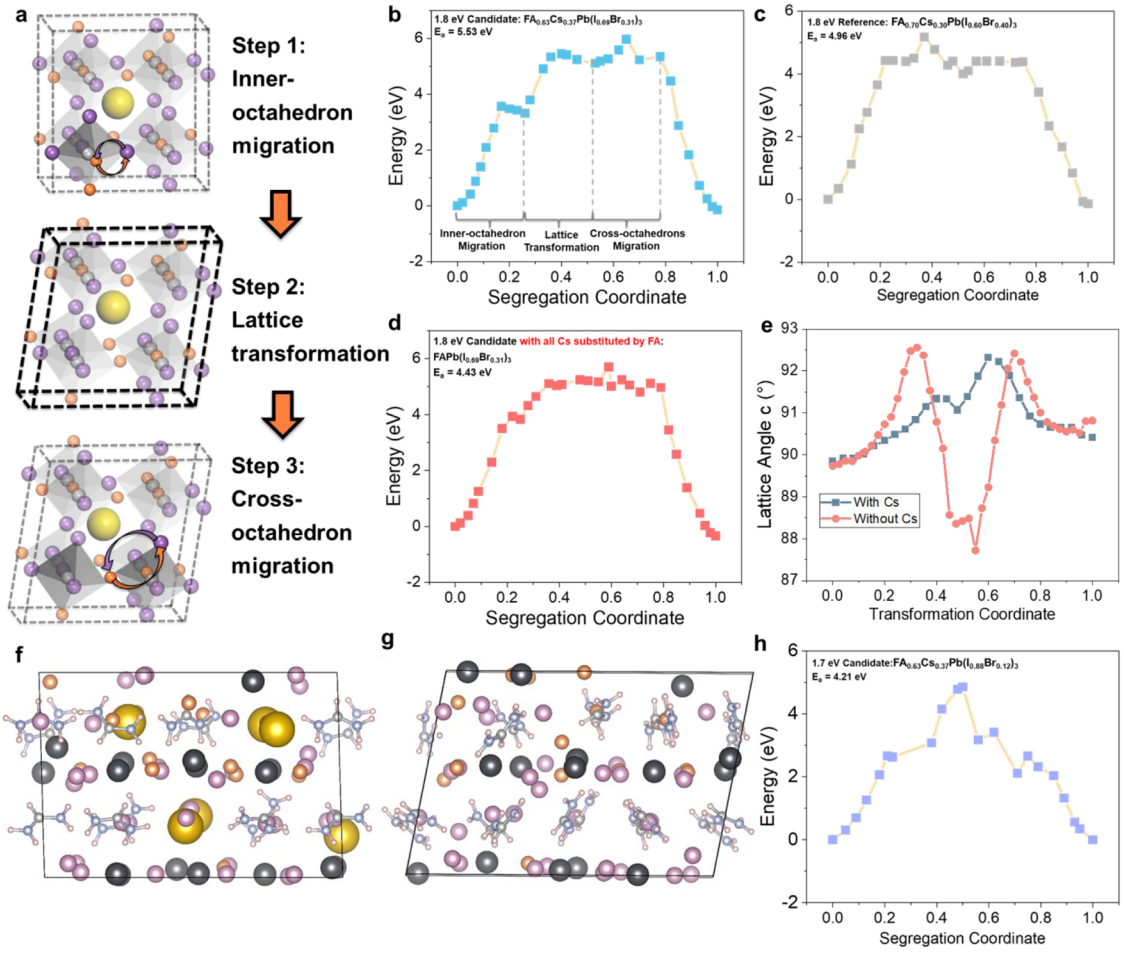

Figure 3. (a) Scheme of the segregation mechanism. (b) Potential energy diagram of the phase segregation process in predicted optimal 1.8 eV perovskites. (c) Potential energy diagram of the phase segregation process in reference 1.8 eV perovskites. (d) Potential energy diagram of the phase segregation process in predicted optimal 1.8 eV perovskites with all Cs substituted by FA. (e) Lattice angle change during the segregation process of predicted and reference perovskites. (f) Transition state of phase segregation process of optimal 1.8 eV perovskite. (g) Transition state of phase segregation process of optimal 1.8 eV perovskite with all Cs substituted by FA. (h) Potential energy diagram of phase segregation process in predicted optimal 1.7 eV perovskite.

of perovskites with this composition. Therefore, we conducted a phase segregation kinetics simulation. The validation test shows that our NN potential could predict an accurate I migration barrier compared with DFT calculation (Figure S10). Then, beginning with the structure indicated in the phase diagram as the initial state of phase segregation, we further separate Br and I in two adjacent regions as the final state of the segregation (Figure S11). Employing the double-ended transition state search methods, we initiated two parallel SSW optimizations simultaneously from the initial state and final state with walking directions pointing toward each other. Upon reaching the same intermediate structure, the initial segregation pathway was successfully linked. Based on the structure with the highest energy in the pathway, more accurate transition states were further located via the constrained Broyden dimer method (CBD).[39] Finally, we obtained a series of structures representing the phase transformation path and normalized the number of each structure from zero to one, which is used to represent the phase segregation coordinate.

According to our calculation, the segregation process proceeds through a step-by-step mechanism (Figure 3a). In the initial step, the Br and I transfer in the original octahedron by exchange of the relative position. Although this step leads to an increase in system energy, the final transition state is still not reached. Then, in the second step, we observe the lattice transformation, i.e., the lattice vector starts to tilt, causing the octahedrons in different layers to no longer overlap with each other in the z direction. Following the lattice transformation, Br and I can diffuse between different octahedrons, allowing the system to reach the highest energy state, i.e., the transition state of the whole segregation process. After the cross-octahedrons diffusion, the perovskite reaches the final state and the lattice recovers back to normal shape with obviously decreasing system energy. Overall, the segregation process has 5.53 eV activation barrier in our predicted 1.8 eV candidate (Figures 3b and S12).

We further calculated another record-breaking 1.8 eV perovskite, $FA_{0.70}Cs_{0.30}Pb(I_{0.60}Br_{0.40})_3$ as reference (Figures 3c and S13−S14).[56] According to our calculation, the same step-by-step phase segregation mechanism is preserved, but the overall activation barrier is lower (4.96 eV). Therefore, our predicted candidate is believed to have better stability. However, the fundamental mechanism underlying the lowered activation barrier remains unclear, as both A sites and X sites' compositions are different in our predicted composition and

https://doi.org/10.1021/jacsau.5c00033
JACS Au 2025, 5, 1771−1780

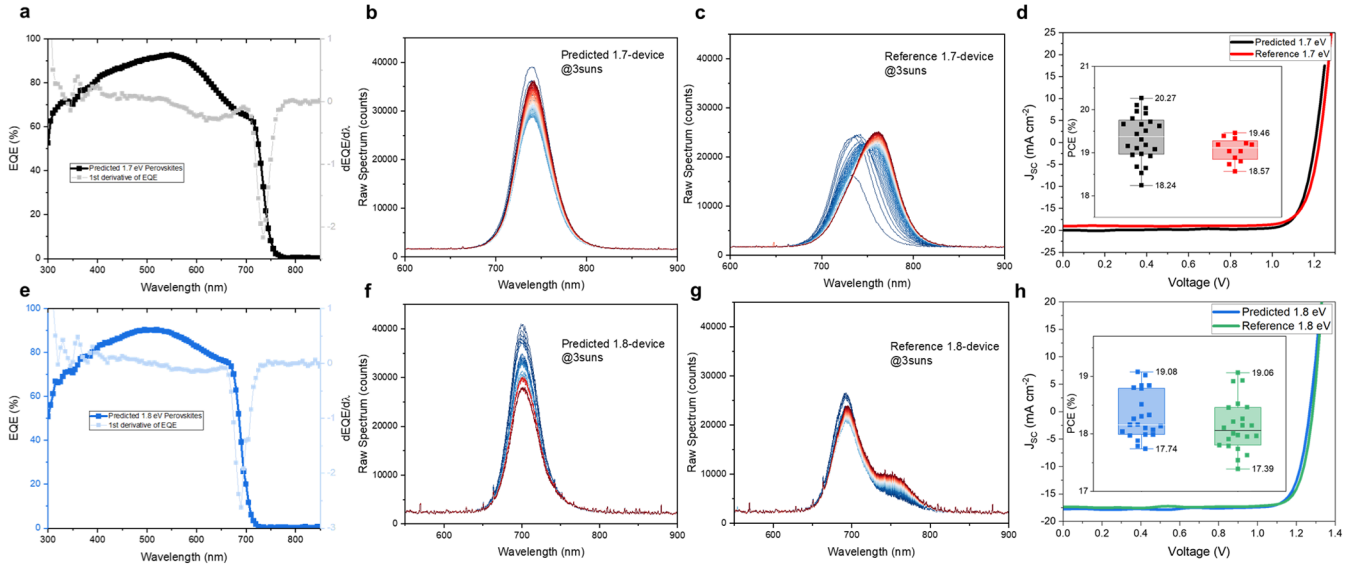

Figure 4. (a) EQE spectra and PV band gap of predicted 1.7 eV perovskites. (b, c) Photoluminescence spectra evolution of predicted and reference 1.7 eV perovskites under 3 times 1-sun AM 1.5G intensity for 17 min. (d) IV performance of predicted 1.7 eV perovskites and reference. The inset is their PCE distribution. (e) EQE spectra and PV band gap of predicted 1.8 eV perovskites. (f, g) Photoluminescence spectra evolution for predicted and reference 1.8 eV perovskites, respectively. (h) IV performance of predicted 1.8 eV perovskites and reference. The inset is their PCE distribution.

reference composition. Therefore, we further investigated the influence of A site composition and B site composition on the overall activation barrier separately.

Based on the 1.8 eV candidate model, we substituted all Cs cations with FA while maintaining the X site composition, resulting in the reference model $FAPb(I_{0.69}Br_{0.31})_3$ (Figure S15). The simulated potential energy diagrams of phase segregation in the reference model are shown in Figures 3d andS16. Interestingly, even with all of the A sites in the lattice occupied by FA, the potential energy diagram still preserves the three-step segregation mechanism. However, the energy state after the lattice transformation is lower compared with the original 1.8 eV candidate, indicating the lattice transformation is facilitated in the absence of Cs. Figure 3e illustrates the difference of the titling degree of lattice vector c during the phase segregation process. When Cs is absent from the lattice, the tilting of lattice vector is more pronounced in the transition states of the reference model (Figure 3f) compared with the 1.8 eV candidate model (Figure 3g). Hence, Cs raises the activation barrier of the phase segregation process by suppressing the lattice transformation of perovskite.

The key feature of the phase segregation process is the concerted migration of two groups of halogen atoms in opposite directions. Essentially, the activation barrier of any migration process would be controlled by two factors: 1. the interaction between the migrated atom and its coordinated atoms, and 2. physical space along the migration path. In our case, the interaction between Pb and I/Br is fixed; therefore, we develop our kinetical modification strategy from the perspective of migration space. Halogen perovskites are known for their soft lattice, which is also revealed by our simulated phase segregation process; i.e., the lattice vector of perovskites could be adjusted easily to open more space for the concerted migration process and lower the segregation activation barrier. However, in our predicted 1.8 eV composition, we propose to add more Cs into the lattice, and we observed lattice transformation is suppressed prominently (Figure 3f,g), which is accompanied by the increased segregation activation barrier. The origin of this phenomenon is that Cs, as a typical inorganic ion, could form a primary ionic bond in the perovskite lattice, which is stronger than the hydrogen-bond-like interaction introduced by organic cation FA. Therefore, with more Cs atoms in the lattice, they can strengthen the lattice and make the lattice more robust to resist the lattice transformation, which makes adding Cs an efficient kinetic suppression strategy for phase segregation.

We took our predicted 1.7 eV candidate as the reference for investigation of the influence of X site anion on the phase segregation (Figure S17). Our predicted 1.7 and 1.8 eV candidates share the same A site composition, while the compositions of the X site are different. As shown in Figures 3h andS18, we could observe that the phase segregation mechanism of the 1.7 eV candidate is totally different from that of the 1.8 eV candidate. The three-step mechanism can no longer be observed, replaced instead by a single atom transfer process in the 1.7 eV candidate. This divergence can be attributed to the reduced amount of Br in the lattice, which eliminates the need for significant lattice transformation to accommodate multiatom concerted transfer. Consequently, the activation barrier decreases significantly as the transfer of a single Br atom entails a low activation barrier. This underscores the importance of the endothermic feature of segregation for low-Br concentration perovskites. Researchers should exercise caution when selecting compositions with low-Br concentration based on our phase diagram, avoiding structures with an exothermic segregation energy.

3.4. The Experimental Verification of Theoretical Prediction

Verification experiments were conducted to validate our theoretical prediction. Perovskites solar cells were synthesized using the predicted 1.8 and 1.7 eV compositions ($FA_{0.63}Cs_{0.37}Pb(I_{0.69}Br_{0.31})_3$ and $FA_{0.63}Cs_{0.37}Pb(I_{0.88}Br_{0.12})_3$) as well as their commonly used reference compositions (1.8 eV: $FA_{0.70}Cs_{0.30}Pb(I_{0.60}Br_{0.40})_3$, 1.7 eV: $FA_{0.83}Cs_{0.17}Pb(I_{0.70}Br_{0.30})_3$)

https://doi.org/10.1021/jacsau.5c00033
JACS Au 2025, 5, 1771−1780

with the same band gap. Firstly, we confirmed the predicted values of PV band gaps (1.69 and 1.80 eV) (Figures 4a,e and S19−S20), which closely matched the calculated values (1.70 and 1.80 eV). This agreement between predicted and calculated band gaps underscores the reliability of both the neural network potential and band gap calculation methods.

Further, we investigated whether our predicted compositions could resist phase segregation using photoluminescence (PL) evolution. Both the predicted 1.7 eV (Figure 4b) and 1.8 eV (Figure 4f) candidates maintained their PL peaks under 3-sun intensity for 17 min, whereas the reference compositions exhibited an obvious red shift of PL peaks (Figure 4c,4g). The 1.7 eV reference composition shows a stronger tendency toward segregation compared with the 1.8 eV reference composition, consistent with our theoretical kinetics results (there are less Br and Cs in the 1.7 eV reference composition, which will lead to a lower activation barrier).

Finally, the I−V tests also indicated that our predicted compositions did not compromise the PV performance compared with reference compositions (Figures 4d,h and S21−S22, Tables S6 and S7). XRD spectra have confirmed the higher phase stability of the predicted 1.7 and 1.8 eV compositions in light conditions (Figure S23 and Table S8). Finally, the overall advantages of the predicted composition have been reflected in the stability test (Figure S24). Further experimental validation on the predicted most stable composition, $FA_{0.90}Cs_{0.10}Pb(I_{0.90}Br_{0.10})_3$ with 1.59 eV band gap, has also shown a good match between theoretical and experimental results (Figure S25). In summary, our experimental verification has proven the theoretical prediction with good matching (Table S9).

4. CONCLUSIONS

In conclusion, our goal is to use machine learning-based theoretical calculations to provide practical guidance and uncover new insights for the preparation or even manufacturing of realistic perovskite solar cells. By mapping out the global phase diagram of hybrid perovskites, we have successfully identified the optimal compositions with different band gaps that can inhibit the phase segregation process, thereby enhancing the stability of perovskite solar cells. Specifically, for perovskites with 1.8 eV band gaps, which are prone to phase segregation, we recommend adding an appropriate amount of Cs and adjusting the I and Br concentrations to raise the barriers to segregation and achieve kinetical control of phase segregation. This study showcases the power of machine learning-driven approaches in maximizing the benefits of compositional engineering by efficiently pinpointing the best compositions. Thus, the integration of machine learning-guided computational design with precise experimental validation is poised to become the standard methodology for developing high-performance perovskite solar cells in the future.

ASSOCIATED CONTENT

Supporting Information

The Supporting Information is available free of charge at https://pubs.acs.org/doi/10.1021/jacsau.5c00033.

Additional computational details, experimental details, materials, and methods, including calculation of phase segregation Gibbs free energy and images of phase segregation process (PDF)

AUTHOR INFORMATION

Corresponding Authors

Zhi-Jian Zhao − *Joint School of National University of Singapore and Tianjin University, International Campus of Tianjin University, Fuzhou 350207, China; Key Laboratory for Green Chemical Technology of Ministry of Education, School of Chemical Engineering & Technology, Tianjin University, Tianjin 300072, China;* orcid.org/0000-0002-8856-5078; Email: zjzhao@tju.edu.cn

Yi Hou − *Department of Chemical and Biomolecular Engineering, National University of Singapore, Singapore 117585, Singapore; Solar Energy Research Institute of Singapore (SERIS), National University of Singapore, Singapore 117574, Singapore;* orcid.org/0000-0002-1532-816X; Email: yi.hou@nus.edu.sg

Jinlong Gong − *Joint School of National University of Singapore and Tianjin University, International Campus of Tianjin University, Fuzhou 350207, China; Key Laboratory for Green Chemical Technology of Ministry of Education, School of Chemical Engineering & Technology, Tianjin University, Tianjin 300072, China; National Industry Education Platform of Energy Storage, Tianjin University, Tianjin 300350, China; Haihe Laboratory of Sustainable Chemical Transformations, Tianjin 300192, China; Collaborative Innovation Center of Chemical Science and Engineering (Tianjin), Tianjin 300072, China; Tianjin Normal University, Tianjin 300387, China;* orcid.org/0000-0001-7263-318X; Email: jlgong@tju.edu.cn

Authors

Ran Luo − *Joint School of National University of Singapore and Tianjin University, International Campus of Tianjin University, Fuzhou 350207, China; Key Laboratory for Green Chemical Technology of Ministry of Education, School of Chemical Engineering & Technology, Tianjin University, Tianjin 300072, China; Department of Chemical and Biomolecular Engineering, National University of Singapore, Singapore 117585, Singapore; Solar Energy Research Institute of Singapore (SERIS), National University of Singapore, Singapore 117574, Singapore*

Xiangkun Jia − *Department of Chemical and Biomolecular Engineering, National University of Singapore, Singapore 117585, Singapore; Solar Energy Research Institute of Singapore (SERIS), National University of Singapore, Singapore 117574, Singapore*

Xiuxiu Niu − *Department of Chemical and Biomolecular Engineering, National University of Singapore, Singapore 117585, Singapore; Solar Energy Research Institute of Singapore (SERIS), National University of Singapore, Singapore 117574, Singapore*

Shunchang Liu − *Department of Chemical and Biomolecular Engineering, National University of Singapore, Singapore 117585, Singapore; Solar Energy Research Institute of Singapore (SERIS), National University of Singapore, Singapore 117574, Singapore;* orcid.org/0000-0002-1990-5737

Xiao Guo − *Department of Chemical and Biomolecular Engineering, National University of Singapore, Singapore 117585, Singapore; Solar Energy Research Institute of Singapore (SERIS), National University of Singapore, Singapore 117574, Singapore;* orcid.org/0000-0001-5478-9789

https://doi.org/10.1021/jacsau.5c00033
JACS Au 2025, 5, 1771−1780

Jia Li − *Solar Energy Research Institute of Singapore (SERIS), National University of Singapore, Singapore 117574, Singapore*

Complete contact information is available at: https://pubs.acs.org/10.1021/jacsau.5c00033

Author Contributions

◆R.L., X.J., and X.N. contributed equally to this work. R.L., Z.-J.Z., Y.H., and J.G. conceived the idea and designed the calculations. Y.H. and J.G. directed and supervised the project. R.L. and Z.-J.Z. constructed the machine learning tool, conducted the simulation, and wrote the manuscript. X.J. and X.N. fabricated and characterized the materials and devices. J.L. assisted with band gap calculation and verification. X.N., S.L., and X.G. were involved in the manuscript review. All authors contributed to discussions and completed the manuscript.

Notes

The authors declare no competing financial interest.

■ ACKNOWLEDGMENTS

Y.H. acknowledges the support from MOE Tier 2 grant (MOE-T2EP10122-0005), the Ministry of Education (Singapore). J.G. acknowledges the support from the National Natural Science Foundation of China (No. 22121004), the Haihe Laboratory of Sustainable Chemical Transformations, and the XPLORER PRIZE. The computational work for this article was fully performed on resources of the National Supercomputing Centre (NSCC), Singapore (https://www.nscc.sg). R.L., X.J., X.N., S.L., X.G., J.L., and Y.H. are affiliated with the Solar Energy Research Institute of Singapore (SERIS), a research institute at the National University of Singapore. SERIS is supported by the National University of Singapore, the National Research Foundation Singapore, the Energy Market Authority of Singapore, and the Singapore Economic Development Board.

■ REFERENCES

(1) Kojima, A.; Teshima, K.; Shirai, Y.; Miyasaka, T. Organometal halide perovskites as visible-light sensitizers for photovoltaic cells. *J. Am. Chem. Soc.* **2009**, *131* (17), 6050−6051.
(2) Kim, J. Y.; Lee, J.-W.; Jung, H. S.; Shin, H.; Park, N.-G. High-efficiency perovskite solar cells. *Chem. Rev.* **2020**, *120* (15), 7867−7918.
(3) Zeng, Y.; Peng, C. W.; Hong, W.; Wang, S.; Yu, C.; Zou, S.; Su, X. Review on Metallization Approaches for High-Efficiency Silicon Heterojunction Solar Cells. *Trans. Tianjin Univ.* **2022**, *28* (5), 358−373.
(4) Unger, E. L.; Kegelmann, L.; Suchan, K.; Sörell, D.; Korte, L.; Albrecht, S. Roadmap and roadblocks for the band gap tunability of metal halide perovskites. *J. Mater. Chem. A* **2017**, *5* (23), 11401−11409.
(5) Wang, Z.; Zeng, L.; Zhu, T.; Chen, H.; Chen, B.; Kubicki, D. J.; Balvanz, A.; Li, C.; Maxwell, A.; Ugur, E.; et al. Suppressed phase segregation for triple-junction perovskite solar cells. *Nature* **2023**, *618* (7963), 74−79.
(6) McMeekin, D. P.; Sadoughi, G.; Rehman, W.; Eperon, G. E.; Saliba, M.; Hörantner, M. T.; Haghighirad, A.; Sakai, N.; Korte, L.; Rech, B.; et al. A mixed-cation lead mixed-halide perovskite absorber for tandem solar cells. *Science* **2016**, *351* (6269), 151−155.
(7) Yang, G.; Ni, Z.; Yu, Z. J.; Larson, B. W.; Yu, Z.; Chen, B.; Alasfour, A.; Xiao, X.; Luther, J. M.; Holman, Z. C.; Huang, J. Defect engineering in wide-bandgap perovskites for efficient perovskite−silicon tandem solar cells. *Nat. Photonics* **2022**, *16* (8), 588−594.
(8) Eperon, G. E.; Leijtens, T.; Bush, K. A.; Prasanna, R.; Green, T.; Wang, J. T.-W.; McMeekin, D. P.; Volonakis, G.; Milot, R. L.; May, R.; et al. Perovskite-perovskite tandem photovoltaics with optimized band gaps. *Science* **2016**, *354* (6314), 861−865.
(9) Leijtens, T.; Bush, K. A.; Prasanna, R.; McGehee, M. D. Opportunities and challenges for tandem solar cells using metal halide perovskite semiconductors. *Nat. Energy* **2018**, *3* (10), 828−838.
(10) Hörantner, M. T.; Leijtens, T.; Ziffer, M. E.; Eperon, G. E.; Christoforo, M. G.; McGehee, M. D.; Snaith, H. J. The potential of multijunction perovskite solar cells. *ACS Energy Lett.* **2017**, *2* (10), 2506−2513.
(11) National Renewable Energy Laboratory. Best Research-Cell Efficiency Chart. 2023 https://www.nrel.gov/pv/cell-efficiency.html.
(12) Eperon, G. E.; Hörantner, M. T.; Snaith, H. J. Metal halide perovskite tandem and multiple-junction photovoltaics. *Nat. Rev. Chem.* **2017**, *1* (12), No. 0095.
(13) Anaya, M.; Lozano, G.; Calvo, M. E.; Míguez, H. ABX_3 perovskites for tandem solar cells. *Joule* **2017**, *1* (4), 769−793.
(14) Yu, Z. J.; Carpenter III, J. V.; Holman, Z. C. Techno-economic viability of silicon-based tandem photovoltaic modules in the United States. *Nat. Energy* **2018**, *3* (9), 747−753.
(15) Bush, K. A.; Frohna, K.; Prasanna, R.; Beal, R. E.; Leijtens, T.; Swifter, S. A.; McGehee, M. D. Compositional engineering for efficient wide band gap perovskites with improved stability to photoinduced phase segregation. *ACS Energy Lett.* **2018**, *3* (2), 428−435.
(16) Zhou, Y.; Jia, Y. H.; Fang, H. H.; Loi, M. A.; Xie, F. Y.; Gong, L.; Qin, M. C.; Lu, X. H.; Wong, C. P.; Zhao, N. Composition-tuned wide bandgap perovskites: From grain engineering to stability and performance improvement. *Adv. Funct. Mater.* **2018**, *28* (35), No. 1803130.
(17) Wen, J.; Zhao, Y.; Liu, Z.; Gao, H.; Lin, R.; Wan, S.; Ji, C.; Xiao, K.; Gao, Y.; Tian, Y.; et al. Steric engineering enables efficient and photostable wide-bandgap perovskites for all-perovskite tandem solar cells. *Adv. Mater.* **2022**, *34* (26), No. 2110356.
(18) Jeon, N. J.; Noh, J. H.; Yang, W. S.; Kim, Y. C.; Ryu, S.; Seo, J.; Seok, S. I. Compositional engineering of perovskite materials for high-performance solar cells. *Nature* **2015**, *517* (7535), 476−480.
(19) Lu, H.; Krishna, A.; Zakeeruddin, S. M.; Gratzel, M.; Hagfeldt, A. Compositional and interface engineering of organic-inorganic lead halide perovskite solar cells. *iScience* **2020**, *23* (8), No. 101359.
(20) Ramadan, A. J.; Oliver, R. D.; Johnston, M. B.; Snaith, H. J. Methylammonium-free wide-bandgap metal halide perovskites for tandem photovoltaics. *Nat. Rev. Mater.* **2023**, *8* (12), 822−838.
(21) Mao, W.; Hall, C. R.; Bernardi, S.; Cheng, Y.-B.; Widmer-Cooper, A.; Smith, T. A.; Bach, U. Light-induced reversal of ion segregation in mixed-halide perovskites. *Nat. Mater.* **2021**, *20* (1), 55−61.
(22) Xu, J.; Boyd, C. C.; Yu, Z. J.; Palmstrom, A. F.; Witter, D. J.; Larson, B. W.; France, R. M.; Werner, J.; Harvey, S. P.; Wolf, E. J.; et al. Triple-halide wide−band gap perovskites with suppressed phase segregation for efficient tandems. *Science* **2020**, *367* (6482), 1097−1104.
(23) Abdi-Jalebi, M.; Andaji-Garmaroudi, Z.; Cacovich, S.; Stavrakas, C.; Philippe, B.; Richter, J. M.; Alsari, M.; Booker, E. P.; Hutter, E. M.; Pearson, A. J.; et al. Maximizing and stabilizing luminescence from halide perovskites with potassium passivation. *Nature* **2018**, *555* (7697), 497−501.
(24) Brennan, M. C.; Draguta, S.; Kamat, P. V.; Kuno, M. Light-induced anion phase segregation in mixed halide perovskites. *ACS Energy Lett.* **2018**, *3* (1), 204−213.
(25) Wang, R.; Mujahid, M.; Duan, Y.; Wang, Z. K.; Xue, J.; Yang, Y. A review of perovskites solar cell stability. *Adv. Funct. Mater.* **2019**, *29* (47), No. 1808843.
(26) Hoke, E. T.; Slotcavage, D. T.; Dohner, E. R.; Bowring, A. R.; Karunadasa, H. I.; McGehee, M. D. Reversible photo-induced trap formation in mixed-halide hybrid perovskites for photovoltaics. *Chem. Sci.* **2015**, *6* (1), 613−617.

(27) Saliba, M. Polyelemental, multicomponent perovskite semiconductor libraries through combinatorial screening. *Adv. Energy Mater.* **2019**, *9* (25), No. 1803754.
(28) Chen, S.; Zhang, L.; Yan, l.; Xiang, X.; Zhao, X.; Yang, S.; Xu, B. Accelerating the screening of perovskite compositions for photovoltaic applications through high-throughput inkjet printing. *Adv. Funct. Mater.* **2019**, *29*, No. 1905487.
(29) Tait, J. G.; Manghooli, S.; Qiu, W.; Rakocevic, L.; Kootstra, L.; Jaysankar, M.; De La Huerta, C. M.; Paetzold, U. W.; Gehlhaar, R.; Cheyns, D.; et al. Rapid composition screening for perovskite photovoltaics via concurrently pumped ultrasonic spray coating. *J. Mater. Chem. A* **2016**, *4* (10), 3792−3797.
(30) Jacobsson, T. J.; Hultqvist, A.; García-Fernández, A.; Anand, A.; Al-Ashouri, A.; Hagfeldt, A.; Crovetto, A.; Abate, A.; Ricciardulli, A. G.; Vijayan, A.; et al. An open-access database and analysis tool for perovskite solar cells based on the FAIR data principles. *Nat. Energy* **2022**, *7* (1), 107−115.
(31) Wei, J.; Tay, Y.; Bommasani, R.; Raffel, C.; Zoph, B.; Borgeaud, S.; Yogatama, D.; Bosma, M.; Zhou, D.; Metzler, D. et al. Emergent abilities of large language models. **2022**, arXiv preprint arXiv:2206.07682. arXiv.org e-Print archive. https://arxiv.org/abs/2206.07682.
(32) Tao, Q.; Xu, P.; Li, M.; Lu, W. Machine learning for perovskite materials design and discovery. *npj Comput. Mater.* **2021**, *7* (1), No. 23.
(33) Ahmadi, M.; Ziatdinov, M.; Zhou, Y.; Lass, E. A.; Kalinin, S. V. Machine learning for high-throughput experimental exploration of metal halide perovskites. *Joule* **2021**, *5* (11), 2797−2822.
(34) Behler, J. Four generations of high-dimensional neural network potentials. *Chem. Rev.* **2021**, *121* (16), 10037−10072.
(35) Huang, S.-D.; Shang, C.; Kang, P. L.; Zhang, X.-J.; Liu, Z.-P. LASP: Fast global potential energy surface exploration. *WIREs Comput. Mol. Sci.* **2019**, *9*, No. e1415.
(36) Huang, S.-D.; Shang, C.; Zhang, X.-J.; Liu, Z.-P. Material discovery by combining stochastic surface walking global optimization with a neural network. *Chem. Sci.* **2017**, *8* (9), 6327−6337.
(37) Zhang, X.-J.; Shang, C.; Liu, Z.-P. Double-ended surface walking method for pathway building and transition state location of complex reactions. *J. Chem. Theory Comput.* **2013**, *9*, 5745−5753.
(38) Zhang, X.-J.; Liu, Z.-P. Reaction sampling and reactivity prediction using the stochastic surface walking method. *Phys. Chem. Chem. Phys.* **2015**, *17*, 2757−2769.
(39) Shang, C.; Liu, Z.-P. Constrained Broyden minimization combined with the dimer method for locating transition state of complex reactions. *J. Chem. Theory Comput.* **2010**, *6*, 1136−1144.
(40) Kresse, G.; Furthmüller, J. Efficient iterative schemes for ab initio total-energy calculations using a plane-wave basis set. *Phys. Rev. B* **1996**, *54*, 11169.
(41) Blöchl, P. E. Projector augmented-wave method. *Phys. Rev. B* **1994**, *50*, 17953.
(42) Kresse, G.; Joubert, D. From ultrasoft pseudopotentials to the projector augmented-wave method. *Phys. Rev. B* **1999**, *59*, 1758.
(43) Perdew, J. P.; Wang, Y. Accurate and simple analytic representation of the electron-gas correlation energy. *Phys. Rev. B* **1992**, *45*, 13244.
(44) Huang, S.-D.; Shang, C.; Kang, P.-L.; Liu, Z.-P. Atomic structure of boron resolved using machine learning and global sampling. *Chem. Sci.* **2018**, *9* (46), 8644−8655.
(45) Behler, J.; Parrinello, M. Generalized neural-network representation of high-dimensional potential-energy surfaces. *Phys. Rev. Lett.* **2007**, *98* (14), No. 146401.
(46) Li, D.; Shi, J.; Xu, Y.; Luo, Y.; Wu, H.; Meng, Q. Inorganic−organic halide perovskites for new photovoltaic technology. *Natl. Sci. Rev.* **2018**, *5* (4), 559−576.
(47) You, J. Stable β-$CsPbI_3$ inorganic perovskites deliver photovoltaic efficiency beyond 18%. *Sci. China Chem.* **2019**, *62* (10), 1267−1268.
(48) Luo, X.; Wu, T.; Wang, Y.; Lin, X.; Su, H.; Han, Q.; Han, L. Progress of all-perovskite tandem solar cells: the role of narrow-bandgap absorbers. *Sci. China Chem.* **2021**, *64*, 218−227.
(49) Chen, H.; Wang, Y.; Fan, Y.; Chen, Y.; Miao, Y.; Qin, Z.; Wang, X.; Liu, X.; Zhu, K.; Gao, F.; Zhao, Y. Decoupling engineering of formamidinium-cesium perovskites for efficient photovoltaics. *Natl. Sci. Rev.* **2022**, *9* (10), No. nwac127.
(50) Zhou, W.; Pan, T.; Ning, Z. Strategies for enhancing the stability of metal halide perovskite towards robust solar cells. *Sci. China Mater.* **2022**, *65* (12), 3190−3201.
(51) Wu, P.; Zhang, F. Recent advances in lead chemisorption for perovskite solar cells. *Trans. Tianjin Univ.* **2022**, *28* (5), 341−357.
(52) Wang, H.; Qin, Z.; Miao, Y.; Zhao, Y. Recent progress in large-area perovskite photovoltaic modules. *Trans. Tianjin Univ.* **2022**, *28* (5), 323−340.
(53) Xing, Z.; Meng, X.; Li, D.; Li, Z.; Gong, C.; Hu, X.; Hu, T.; Chen, Y. Multi-environment phase stabilization by lattice reinforcement for efficient perovskite solar cells. *Sci. China Mater.* **2023**, *66* (7), 2573−2581.
(54) Jiang, X.; Zhou, Q.; Lu, Y.; Liang, H.; Li, W.; Wei, Q.; Pan, M.; Wen, X.; Wang, X.; Zhou, W.; et al. Surface heterojunction based on n-type low-dimensional perovskite film for highly efficient perovskite tandem solar cells. *Natl. Sci. Rev.* **2024**, *11* (5), No. nwae055.
(55) Liu, X.; Chen, L.; Yu, Y.; He, D.; Shai, X.; Zhang, S.; Zhang, Z.; Feng, J.; Yi, L.; Chen, J. Advancements of highly efficient perovskite based tandem solar cells *Sci. China Mater.* 2024 DOI: 10.1007/s40843-024-3076-3.
(56) Lin, R.; Xu, J.; Wei, M.; Wang, Y.; Qin, Z.; Liu, Z.; Wu, J.; Xiao, K.; Chen, B.; Park, S. M.; et al. All-perovskite tandem solar cells with improved grain surface passivation. *Nature* **2022**, *603* (7899), 73−78.

https://doi.org/10.1021/jacsau.5c00033
JACS Au 2025, 5, 1771−1780